Mon. Not. R. Astron. Soc. **391,** 1545–1558 (2008) doi:10.1111/j.1365-2966.2008.13953.x

The Arcminute Microkelvin Imager[★]

AMI Consortium: J. T. L. Zwart,[†] R. W. Barker, P. Biddulph, D. Bly, R. C. Boysen, A. R. Brown, C. Clementson, M. Crofts, T. L. Culverhouse,[‡] J. Czeres, R. J. Dace, M. L. Davies, R. D'Alessandro, P. Doherty, K. Duggan, J. A. Ely, M. Felvus, F. Feroz, W. Flynn,[§] T. M. O. Franzen, J. Geisbüsch, R. Génova-Santos,[¶] K. J. B. Grainge, W. F. Grainger,[‖] D. Hammett, R. E. Hills,[★★] M. P. Hobson, C. M. Holler[††], N. Hurley-Walker, R. Jilley, M. E. Jones,[††] T. Kaneko, R. Kneissl[‡‡], K. Lancaster,[§§] A. N. Lasenby, P. J. Marshall,[¶¶] F. Newton, O. Norris,[§] I. Northrop, D. M. Odell, G. Petencin,[‖‖] J. C. Pober, G. G. Pooley, M. W. Pospieszalski,[‖‖] V. Quy, C. Rodríguez-Gonzálvez, R. D. E. Saunders, A. M. M. Scaife, J. Schofield, P. F. Scott, C. Shaw, T. W. Shimwell, H. Smith, A. C. Taylor,[††] D. J. Titterington, M. Velić,[***] E. M. Waldram, S. West, B. A. Wood and G. Yassin[††]

Astrophysics Group, Cavendish Laboratory, J. J. Thomson Avenue, Cambridge CB3 0HE

Accepted 2008 September 12. Received 2008 September 12; in original form 2008 July 3

ABSTRACT

The Arcminute Microkelvin Imager is a pair of interferometer arrays operating with six frequency channels spanning 13.9–18.2 GHz, for observations on angular scales of 30 arcsec–10 arcmin and for declinations greater than $-15°$; the Small Array has a sensitivity of $30\,\mathrm{mJy\,s^{-1/2}}$ and the Large Array has a sensitivity of $3\,\mathrm{mJy\,s^{-1/2}}$. The telescope is aimed principally at Sunyaev–Zel'dovich imaging of clusters of galaxies. We discuss the design of the telescope and describe and explain its electronic and mechanical systems.

Key words: instrumentation: interferometers – telescopes – galaxies: clusters: general – cosmic microwave background – cosmology: observations – radio continuum: general.

1 INTRODUCTION

Clusters of galaxies are the best samplers of matter on the largest scales and are sensitive probes of structure formation, both in the linear regime of growth and when merging, shocking and gradual virialization occur. Determining the structures and physics of clusters, their mass function and their evolution is therefore of basic importance.

Observationally, however, relatively little is known about the properties of the cluster population at redshifts $z \gtrsim 1$, due to the fundamental problem of the dimming of surface brightness with redshift. Optical observations suffer from confusion from foreground galaxies, and both optical and X-ray observations suffer from biases towards strong concentrations of mass such as clumps.

[★] We request that any reference to this paper cites 'AMI Consortium: Zwart et al. 2008'.

[†] Issuing author: jtlz2@mrao.cam.ac.uk

[‡] Present address: Kavli Institute for Cosmological Physics, University of Chicago, 5640 South Ellis Avenue, Chicago, IL 60637, USA.

[§] Present address: The University Chemical Laboratory, Lensfield Road, Cambridge CB2 1EW.

[¶] Present address: Instituto de Astrofísica de Canarias, 38200 La Laguna, Tenerife, Canary Islands, Spain.

[‖] Present address: Department of Physics, Columbia University, 538 W. 120th Street, New York, NY 10027, USA.

[★★] Present address: Joint ALMA Office, Av El Golf 40, Piso 18, Santiago, Chile.

[††] Present address: Astrophysics Group, Department of Physics, Denys Wilkinson Building, Keble Road, Oxford OX1 3RH.

[‡‡] Present address: MPI für Radioastronomie, Auf dem Hügel 69, D-53121 Bonn, Germany.

[§§] Present address: Astrophysics Group, H. H. Wills Physics Laboratory, Royal Fort, Tyndall Avenue, Bristol BS8 1TL.

[¶¶] Present address: UC Santa Barbara, Santa Barbara, CA 93106, USA.

[‖‖] Present address: NRAO Technology Center, 1180 Boxwood Estate Road, Charlottesville, VA 22903, USA.

[***] Present address: Spatial Technology Ltd, 1 Quayside, Cambridge CB5 8AB.

Ionized matter at any redshift out to recombination will inverse-Compton scatter the cosmic microwave background (CMB) radiation and so imprint spatial fluctuations upon it. Hot ionized gas in the deep potential wells of galaxy clusters (statistically) up-scatters CMB photons passing through it, giving rise to the Sunyaev–Zel'dovich (SZ) effect (Sunyaev & Zeldovich 1970, 1972; see e.g. Birkinshaw 1999; Carlstrom, Holder & Reese 2002 for reviews); at frequencies below 217 GHz, one sees a decrease in the CMB temperature towards the cluster. This dip in brightness temperature $\Delta\ T$ is given in the Rayleigh–Jeans region by $\Delta T = -2yT_{\rm CMB}$, where the Comptonization parameter $y = \int n_{\rm e}\sigma_{\rm T}(k_{\rm B}T_{\rm e})/(m_{\rm e}c^2)\,{\rm d}l$, $\sigma_{\rm T}$ is the Thomson cross-section, l is the line-of-sight path and $m_{\rm e}$, $n_{\rm e}$ and $T_{\rm e}$ are, respectively, the electron mass, density and temperature. The dip $\Delta\ T$ is thus proportional to the line integral of pressure but does *not* depend on redshift z. One way of seeing this is that in such a inverse-Compton scattering process, the power lost by the electrons and given to the CMB photons is proportional to the energy density of the CMB radiation which is proportional to $(1 + z)^4$; this exactly cancels out the cosmological drop in bolometric surface brightness proportional to $(1 + z)^{-4}$. This is an extremely important result – one can get *directly* to high redshift using SZ without any intermediate steps.

The total SZ decrement in flux density, $\Delta S_{\rm SZ}$, is proportional to the integral of the brightness temperature $\int \Delta T_{\rm SZ}\,{\rm d}\Omega$ over the solid angle Ω subtended by the cluster. Thus $\Delta S_{\rm SZ} \propto D_{\rm A}^{-2}\int n_{\rm e}T_{\rm e}\,{\rm d}V$, where $D_{\rm A}$ is the angular-size distance and d V is an element of volume. For concordance cosmologies, for redshifts between, say, 0.3 and 3, $D_{\rm A}$ is only weakly dependent on redshift. Since, for the Einstein–de-Sitter and concordance cosmologies, $D_{\rm A}$ is always a weaker function of redshift than luminosity distance $D_{\rm L}$, SZ clusters will have a selection function that is much less dependent on redshift than most self-luminous objects. $\Delta\ S_{\rm SZ}$ measures the total thermal energy of the cluster, and since temperature is strongly correlated to mass (e.g. $T \propto M^{2/3}$ for a population of clusters, modelled as virialized gravitationally collapsed systems), the integrated SZ flux density measures gas mass directly, and with less bias to concentrated structure than optical or X-ray measurements. Detailed studies of clusters in SZ and other wavebands will help to establish the cosmological relationship between M and T and the thermal history of the cluster, and will help to calibrate the cluster scaling relations.

These points immediately emphasize the importance of SZ surveys for clusters. These have long been advocated (see e.g. Korolev, Sunyaev & Yakubtsev 1986; Bond & Myers 1992; Bartlett & Silk 1994) and it is now widely recognized that such surveys are key measurements for cosmology. For example, it is critical to measure and understand the comoving number density of clusters, $N(M, z)$, as a function of mass M and redshift. $N(M, z)$ is a very strong function of the key cosmological parameter σ_8 – the density contrast on scales of 8 h^{-1} Mpc now – and of the physics of cluster assembly.

The X-ray flux from a cluster is proportional to $n_{\rm e}^2 f(T_{\rm e})$, where $f(T_{\rm e})$ is not a strong function of $T_{\rm e}$. The SZ flux is proportional to $n_{\rm e}\ T_{\rm e}$, so the combination of good X-ray and SZ data on a cluster gives robust determinations of density and temperature distributions and the related physics. Since the SZ flux density is proportional to the integrated gas pressure rather than to the density squared, it is relatively more sensitive to the outer parts of clusters than are X-rays, and not biased towards dense regions.

All these points also emphasize the importance of pointed, high-resolution SZ observations of clusters known from X-ray, optical/infrared (IR) or SZ surveying, as well as X-ray/optical/IR observations of SZ-selected targets. For example, cluster observations from *XMM–Newton* and *Chandra* show clear entropy structures in a cluster's gas, with contact discontinuities and sloshing motions (see e.g. Rossetti et al. 2007), and bubbling and reheating of cooling gas by Fanaroff–Riley I (FRI) radio jets of low luminosity but considerable bulk kinetic power (e.g. Sanders & Fabian 2007). Observations in different wavebands tease out different selection effects.

The first unequivocal SZ detections were made using the Owens Valley Radio Observatory (OVRO) 40-m telescope and the National Radio Astronomy Observatories (NRAO) 140-foot telescope (Birkinshaw, Gull & Moffet 1981; Birkinshaw, Gull & Hardebeck 1984; Uson 1986), and the first SZ image was obtained with the Ryle Telescope (RT; Jones et al. 1993). The RT and OVRO/Berkeley–Illinois–Maryland Association (BIMA) interferometers have since then made many SZ observations of known clusters (see e.g. Carlstrom, Joy & Grego 1996; Grainge et al. 1996, 2002a,b; Grego et al. 2000; Patel et al. 2000; Reese et al. 2000, 2002; Joy et al. 2001; Cotter et al. 2002a,b; Grainger et al. 2002; Saunders et al. 2003; Jones et al. 2005; Bonamente et al. 2006; LaRoque et al. 2006). Each of these observations has however been long (1–60 d), because even the shortest baselines resolved out most of the SZ signal: some 90 per cent of the SZ flux from a massive cluster at $z = 0.2$ is missed by a 600λ baseline, the smallest possible given the existing dish sizes of the RT and OVRO/BIMA.

Several other instruments have successfully observed the SZ effect, including the OVRO 5.5-m telescope (Herbig et al. 1995), Sunyaev–Zel'dovich Infrared Experiment (SuZIE; Holzapfel et al. 1997), Arcminute Cosmology Bolometer Array Receiver (ACBAR; Cantalupo et al. 2002), Cosmic Background Imager (CBI; Udomprasert et al. 2004), Very Small Array (VSA; Lancaster et al. 2005) and One Centimetre Receiver Array (OCRA; Lancaster et al. 2007). It has, however, long been clear that, for detailed imaging and blind surveying, a new generation of fast SZ imagers is required, with angular scale and brightness temperature sensitivities far better matched to the features of interest in clusters. Of course, such instruments should also be able to measure the CMB power spectrum at high angular scales ($\ell > 2000$) and thus investigate the origins of, for example, the excess CMB power detected by CBI (Mason et al. 2003). They also are pertinent to the search for other non-Gaussian features such as topological defects.

Accordingly, we have designed, built and now operate the Arcminute Microkelvin Imager (AMI; see Kneissl et al. 2001; AMI Collaboration 2006), a pair of interferometer arrays operating around 15 GHz near Cambridge, UK. Before describing AMI in detail, we next review other new SZ instruments, as well as the advantages and disadvantages of interferometers.

1.1 Fast SZ instruments

Several powerful SZ instruments are now coming online. The majority are direct-imaging, focal-plane arrays of bolometers, operating at frequencies above 90 GHz: Atacama Cosmology Telescope (ACT; e.g. Kosowsky 2006) in Chile uses a 6-m antenna with a resolution of 1.44 arcmin at e.g. 150 GHz; Atacama Pathfinder Experiment (APEX; e.g. Dobbs et al. 2006) in Chile has a 12-m antenna with 1.0-arcmin resolution at e.g. 150 GHz; South Pole Telescope (SPT; e.g. Ruhl et al. 2004) at the South Pole has a 10-m antenna with resolution of 1.06 arcmin at e.g. 150 GHz; the *Planck* satellite, due for launch in 2009 January, will detect clusters in SZ over the whole sky, but detecting distant clusters will be challenging due to its limited resolution (see e.g. Geisbüsch, Kneissl & Hobson 2005).

There are also three interferometers, operating at lower frequencies: AMI, see below; Array for Microwave Background Anisotropy

(AMiBA; see e.g. Li et al. 2006) in Hawaii, with the array co-mounted on a hexapod and currently at 90 GHz and the Sunyaev–Zel'dovich Array (SZA; see e.g. Muchovej et al. 2007) in California with 3.5-m diameter antennas – the SZA has been operating at 30 GHz with a resolution of 1 arcmin and will be operated at 90 GHz as part of Combined Array for Research in Millimetre-wave Astronomy (CARMA; www.mmarray.org).

1.2 Advantages and disadvantages of interferometers

Interferometry has some significant advantages for observations where high sensitivity and low systematics are required (see e.g. Church 1995; Lay & Halverson 2000; Lancaster 2004; Zwart 2007).

(i) Stability of receivers. Short-term fluctuations in the gains of the front-end amplifiers are uncorrelated and therefore contribute only to the random noise.

(ii) Emission from the atmosphere is largely uncorrelated (provided the antenna beams do not overlap within the troposphere), and associated receiver power fluctuations are completely uncorrelated and thus contribute only to the system noise.

(iii) Fringe-rate filtering. Astronomical signals are modulated at the celestial fringe rate by the Earth's rotation. Unwanted interference from sources at terrestrial fringe rates, such as ground spill and geostationary satellite broadcasts, can be attenuated. Residual correlated atmospheric emission also has very little power in components that are synchronous with the astronomical fringe rate.

(iv) Each interferometer baseline responds to only a narrow range of spatial frequencies; as well as filtering out the large-scale atmospheric signals this can be used to e.g. minimize the response to the primary CMB anisotropies while retaining sensitivity to clusters. Indeed, interferometers have zero response to power which is uniformly spatially distributed (e.g. most of the atmospheric emission and the CMB average temperature), and hence do not respond to temporal fluctuations in that power.

(v) Foreground removal. Radio point sources can be detected by baselines chosen to be sensitive to smaller angular scales. This allows them to be measured simultaneously and subtracted.

The main disadvantages of interferometers are complication (with the number of correlators going as the square of the number of detector elements) and a restriction on observing frequency. The SZ decrement has a maximum amplitude in intensity at approximately 130 GHz; contaminating synchrotron emission from radio sources *generally* decreases with increasing frequency (falling in temperature as $\nu^{-(\alpha+2)}$ where α is the flux-density spectral index), although the effect of dust in galaxies on SZ observation at, say, 150 GHz is presently uncertain. Radio interferometers employing heterodyne receivers have costs and amplifier noise that rise with frequency, which in the past has limited interferometers to observing frequencies of around 30 GHz.

1.3 The rest of this paper

We next describe the design of the instrument (Section 2), including the choice of frequency and the need for two interferometric arrays, the Large Array (LA) and the Small Array (SA). We describe the antennas, optics and array configurations of the SA and LA in Section 3. The amplifiers and cryostats are outlined in Section 4, with the signal chain expounded in Section 5. Section 6 covers correlator and readout systems, and Section 7, the telescope control systems. Some lessons learned are outlined in Section 8.

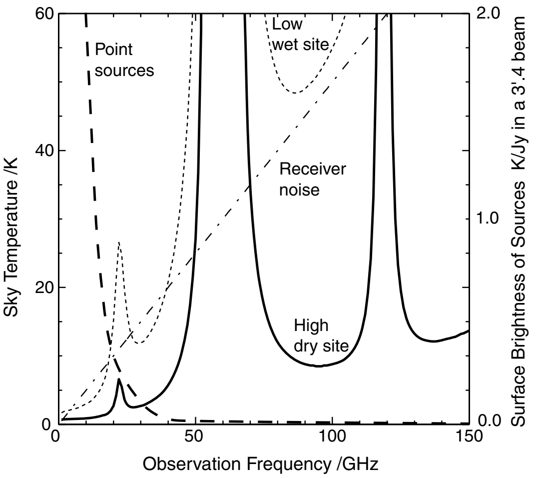

Figure 1. The contribution of atmospheric emission to system temperature as a function of frequency. The upper dashed curve is for a sea-level site like Cambridge. The lower solid line is for a high, dry site like Mauna Kea. The typical noise temperature of a HEMT amplifier is also plotted. The thick dashed curve is the brightness temperature of an unresolved 1-Jy source (with a spectral index of 0.7) at 15 GHz in a 3.4-arcmin beam (from Kaneko 2006, after Jones 2002).

2 AMI BASIC DESIGN

2.1 Choice of frequency

The AMI frequencies are chosen to give the highest ratio of SZ signal to total noise, constrained by our need to minimize cost. The competing noise terms are the receiver noise and sky background, which rise with frequency, and the effect of radio source confusion, which falls with frequency. The temperature of the atmosphere at a low-altitude site rises quite steeply between $\approx$5 K at 15 GHz and $\approx$30 K at 30 GHz (see Fig. 1). Experience from the 5-km telescope (Ryle 1972), CAT (Robson et al. 1994) and the initial testing of the VSA at 30 GHz at the Lord's Bridge site near Cambridge, UK (Rusholme 2001), showed that observations at frequencies up to 18 GHz are achievable from there, but sensitive 30-GHz observations are ruled out. However, the existence of the Ryle Telescope (which has eight 13-m antennas) on this site means that high sensitivity and resolution observations of the confusing point sources are possible. Constructing a higher frequency instrument on a remote site (there is none suitable in the UK) would have been very much more expensive. Hence we chose to operate in the band 12–18 GHz, the upper limit being set by the presence of the 22-GHz water line, and the bandwidth set by the use of single-moded waveguide and feeds. Note that the precise frequency range and bandwidth are dependent on the dimensions of commercially available waveguide.

2.2 The two arrays

The choice of such frequencies for SZ observation leads immediately to the requirement to provide much higher flux sensitivity on longer baselines to remove the small angular size radio sources which would otherwise obscure the SZ (see e.g. Grainge et al. 1996; Grainger et al. 2002; Lin et al. 2008). The eight 13-m antennas of the RT – the RT itself being a radical receiver- and signal-processing upgrade of the 5-km telescope – form the basis of source removal. We thus arrived at a two-array design, with the SA sensitive to SZ and contaminant sources, and the LA for robust removal of the

Table 1. AMI technical summary.

	SA	LA
Antenna diameter	3.7 m	12.8 m
Antenna efficiency	0.75	0.67
Number of antennas	10	8
Number of baselines	45	28
Baseline lengths (current)	5–20 m	18–110 m
Primary beam (15.7 GHz)	20.1 arcmin	5.5 arcmin
Synthesized beam	≈3 arcmin	≈30 arcsec
Flux sensitivity	30 mJy s$^{-1/2}$	3 mJy s$^{-1/2}$
Observing frequency	13.9–18.2 GHz	
Bandwidth	4.3 GHz	
Number of channels	6	
Channel bandwidth	0.72 GHz	
System temperature	25 K	
Declination range	$> -15°$	$> -20°$
Elevation limit	+20°	+5°
Polarization measured	$I + Q$	

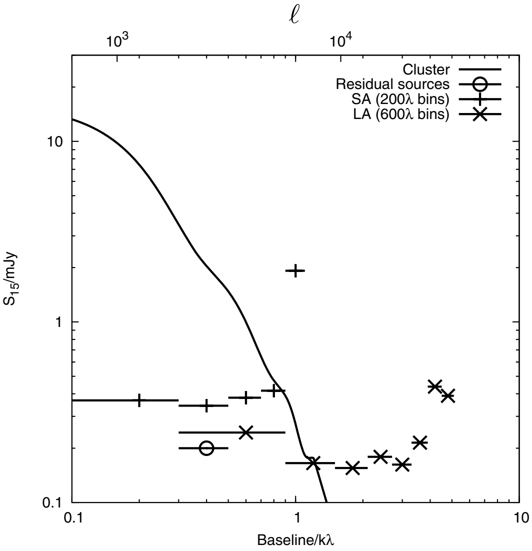

Figure 2. This figure illustrates some of the issues affecting the sensitivity of AMI to an SZ signal, with angular scale $\theta \simeq (180°/\ell)$. The solid line indicates the SZ signal received by the SA from a typical rich cluster (in this case modelled as a spherically symmetric isothermal β profile with core radius 60 arcsec, central electron temperature 7 keV and density 0.01 cm^{-3} at $z = 0.171$). The vertical crosses indicate the 1σ flux sensitivity of the SA in 200λ bins for an 8-h observation; diagonal crosses show the 1σ flux sensitivity of the LA (with 600λ bins) for an observation of the same duration and rastered in order to cover the same sky area; for both the SA and the LA, the horizontal lines denote the range of baselines contributing to each cross. The circle indicates the confusion from remnant unsubtracted sources in a 2-arcmin full width at half-maximum (FWHM) synthesized beam, with source count from Waldram et al. (2003), and assuming that all sources above a limiting flux density $S_{\rm lim} = 1.9$ mJy have been removed; the LA can measure the fluxes of each of these sources at $\geq 5\sigma$ in about 15 min over an SA field-of-view. Contamination by primordial CMB signals is not significant for AMI observations of clusters at $z > 0.1$ and $M_{\rm tot} > 10^{14}$ M$_\odot$.

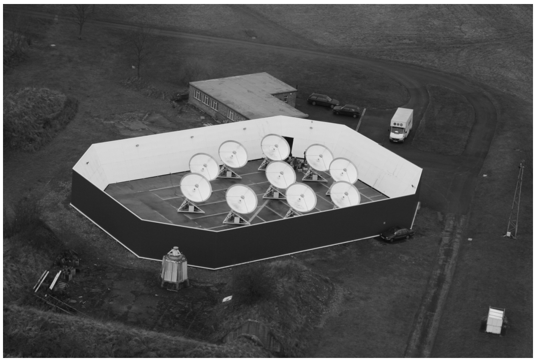

Figure 3. SA from the south-east. The correlator is in the building behind. The enclosure floor is now covered in aluminium.

sources. Note, however, that the flux sensitivity of the LA and its particular range of baselines combine to allow it also to map SZ at high resolution.

The details of the SA and LA are outlined in Table 1 and sensitivity illustrated in Fig. 2. Note that maintaining full angular resolution over the field of view of each of these arrays would be impossible with a single 6-GHz-wide channel because of chromatic aberration. Hence we split the signal into eight 0.75-GHz-wide channels, which results in acceptably small chromatic aberration at the field edge at full array resolution.

3 ANTENNAS AND OPTICS

The SA and LA are shown in Figs 3 and 4. The SA subsystems are illustrated in Fig. 5 (the LA subsystems are very similar).

3.1 Small Array

The SA consists of 10 3.7-m diameter antennas surrounded by an aluminium groundshield. These are described in the following subsections.

3.1.1 Enclosure and mount

The antennas of the SA are designed around commercially available spun 3.7-m parabolic reflectors. These are made by fixing an aluminium sheet to the centre of a paraboloidal former; the whole assembly is then spun about its symmetry axis and the sheet is pressed on to the former from the centre outwards with a roller. The rms surface accuracy of these single-piece reflectors is better than 0.3 mm and the cost savings over machined or segmented dishes are large. Like the existing LA dishes, the SA dishes are equatorially mounted with a Cassegrain focus (Fig. 6). An advantage of an equatorial mount is that the observed angle of polarization is constant over the whole observation. Point sources measured by the LA can then be directly subtracted from the SA data.

Each dish has a circular tube rolled into the rim to provide stiffness. The backing structure consists of a lattice of 16 tubes connecting eight points on the rim to the vertices of an octagonal frame, which is connected in turn to the mount structure. The dish surface is thus suspended from the rim with no loading other than its own weight. To prevent stresses from being built in to the dishes during assembly, the fittings at the ends of the lattice tubes were free to slide, and were then epoxied while the octagon frame was suspended above the back surface of the dish on a jig. The antennas can track over ±6 h in hour angle (HA) and $-15°$ to $+90°$ in declination (δ). In normal use, an elevation limit of 20° restricts the HA range to ±2.5 h at $\delta = -10°$.

Each antenna is designed to be able to observe in up to 40 knots (75 km h^{-1}) of wind, with an rms pointing accuracy of 20 arcsec,

Figure 4. LA from the north-east. The correlator is in the central hut. The railway track, which runs diagonally across the photograph, is approximately east-west. Four antennas are moveable along the track.

and survive up to 100 knots (180 km h^{-1}). The antennas are housed in a reflective aluminium enclosure (with internal dimensions of $40 \times 28\,\mathrm{m}^2$ at ground level and height 4.5 m) to reduce ground spill and terrestrial interference, and to offer additional protection from wind.

3.1.2 Optics

The aperture efficiency of classical Cassegrain systems is only in the range of 70–75 per cent. Shaped primary reflectors (Galindo 1964) are expensive to produce but have much better efficiency; for example the efficiency of the LA calculated at 15 GHz is 89 per cent (excluding the struts that support the secondary reflector; see below). Our principal requirements were an efficiency of over 80 per cent over most of the band with low sidelobes.

A rolled-edge Cassegrain system was developed to achieve these criteria (Holler et al. 2008). An oversized secondary reflector improves the aperture efficiency but also increases the sidelobe level. These sidelobes can pick up emission from the warm ground and degrade the system temperature, as well as introducing spurious signals. Rolling the secondary reflector's edge towards the primary reflector ensures that rays entering the horn come from the cold sky rather than from the ground. Unlike a shaped Cassegrain system, the phase front in the rolled-edge Cassegrain system is not uniform, but the distortion is negligible at 15 GHz. The residual sidelobes add about 6 K to the system temperature.

An additional 15-cm rim around the primary reflector, mounted at 45° to the optical axis, redirects part of the sidelobes to the sky and reduces the ground spill to below 2 K. The aperture efficiency is 81–82 per cent between 12.5 and 15 GHz, falling to 75 per cent at 17.5 GHz. Sidelobes at $>30^\circ$ are suppressed by at least 60 dB.

The secondary reflector is supported by three struts; scattering from the struts is reduced by shaped deflectors fitted to the struts to redirect rays to the sky, giving a further reduction in ground spill.

The SA is configured along a quasi-Reuleaux triangle (Keto 1997) along the north–south direction with a central antenna (Fig. 7). Empirically, this offered the best compromise between temperature sensitivity, coverage in the *uv* plane (which dictates the synthesized beam shape) and minimized antenna-to-antenna shadowing within the confines of the enclosure. However, for dedicated low-declination observations, stretching the array along the north–south direction significantly improves the *uv* coverage.

3.1.3 Alignment

A north–south line was generated, and marked on brass plates on the floor of the enclosure, from observations of Polaris in 2005 March. The SA antennas were aligned in azimuth to this line with a theodolite and aligned vertically using a digital clinometer. The antennas were aligned to within 1 arcmin, with further corrections made astronomically.

The antennas can be repositioned e.g. to optimize *uv* coverage for a particular target or field. To facilitate this, we have installed an optical alignment system that allows each antenna to be realigned rapidly to within a few arcsec of its original orientation using a mirror fixed to its structure. The system employs a Taylor Hobson Micro-Alignment Telescope, operating in autocollimation mode, in conjunction with a moveable pentaprism.

3.2 Large Array

The 5-km telescope was an approximately east–west linear array of eight 13-m diameter Cassegrain antennas operating at 2.7, 5 and 15 GHz, with $\leq$20-MHz bandwidth, to achieve a maximum resolution of 0.7 arcsec; it was designed for state-of-art imaging of radio galaxies, radio quasars and supernova remnants. In 1985, work began on equipping it with cryogenically cooled receivers and 0.35-GHz bandwidth (with much narrower individual channels to avoid chromatic aberration). This created the RT in order to do, among other things, SZ imaging with its five closely packable antennas. We have now moved all eight antennas into a close, two-dimensional array and have fitted new receivers and signal processing.

3.2.1 Array configuration

The LA antenna configuration is shown in Fig. 8. Antennas 1–4 are moveable along a railway track and the positions of the remaining antennas are fixed. Antennas 6–8, which were the most westerly of the 5-km telescope, have been placed to allow the array to observe equatorial fields without a loss of resolution.

4 CRYOGENIC RECEIVERS

The first-stage amplifiers (Section 4.1) are identical for the SA and LA, but the cryostats and horns are very different (Sections 4.2 and 4.3).

4.1 Low-noise amplifiers

The first-stage amplifiers are an 8–18 GHz (optimized for 12–18 GHz as standard) design used as the intermediate frequency (IF) amplifier in the NRAO 80–95 GHz Very Long Baseline Array (VLBA) receivers and elsewhere (Webber & Pospieszalski 2002; Pospieszalski 2005). Each amplifier contains three InP high electron mobility transistors (HEMTs). The amplifiers are intrinsically low noise, with a minimum noise temperature of about 6 K when cooled to 20 K.

The second-stage amplifiers are either earlier generation NRAO HEMT designs (recycled from the CAT and RT) or internally biased amplifiers manufactured by Avantek; all are operated at ambient temperature. We can afford to run the second-stage amplifiers warm because the 30-dB gain of the front-end amplifiers is so high (see Fig. 11). The bias of each front-end HEMT is externally tunable from a 'bias box'.

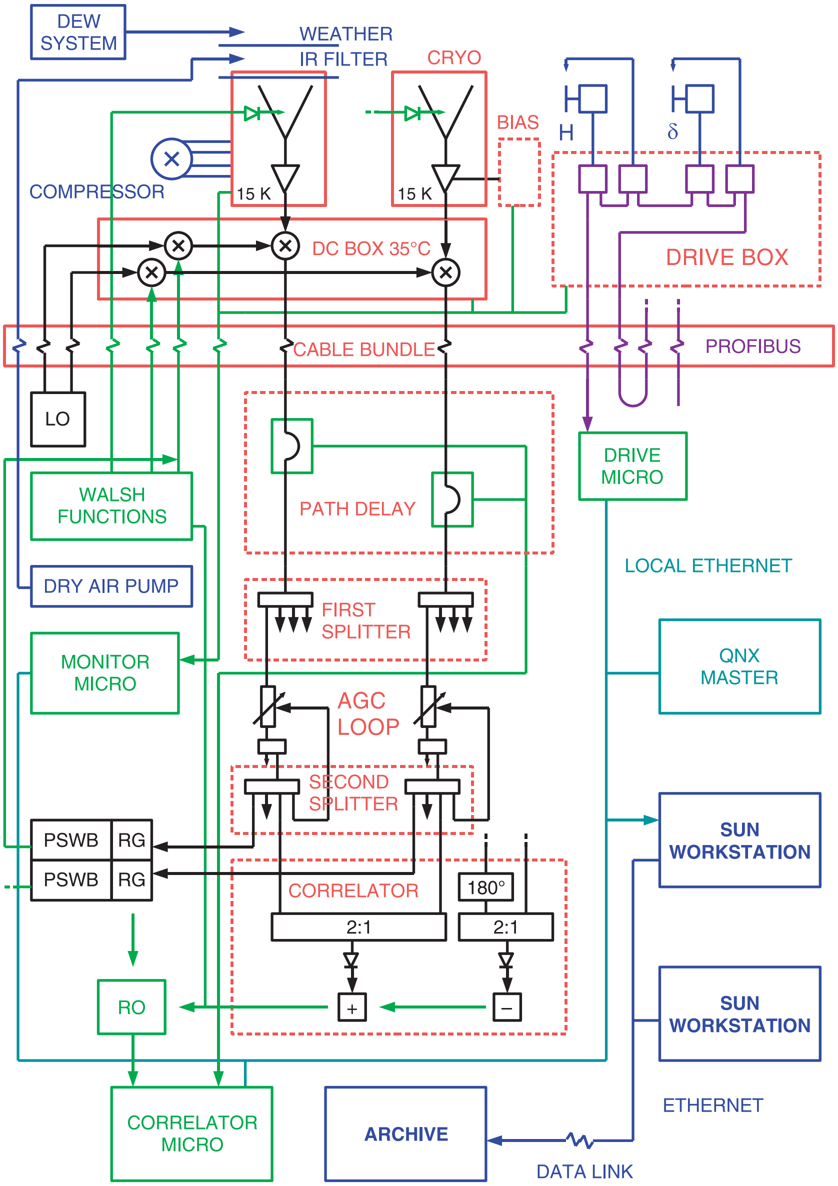

Figure 5. SA subsystems. Equalizers and all amplifiers (apart from the front-end amplifiers) are omitted from this diagram. AGC is automatic gain control, DC is downconversion, LO is the local oscillator, PSWB is phase-switch balance, RG is the system temperature monitor ('rain gauge') and RO is correlator readout. The LA subsystems are essentially identical (see text for details), but in particular: there is no dew system, dry-air pump or infrared filter, in part because the horn extends beyond the cryostat; the drive system does not use the Profibus interface, with instead one drive microprocessor per antenna; monitoring is carried out by each antenna's drive microprocessor and there is no QNX operating system (see Section 7).

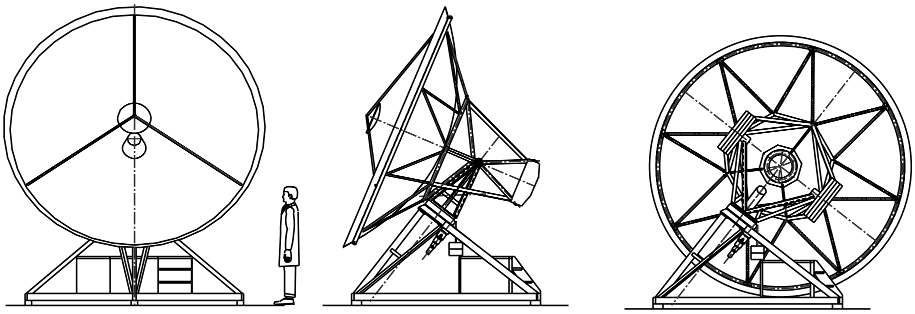

Figure 6. A single SA antenna.

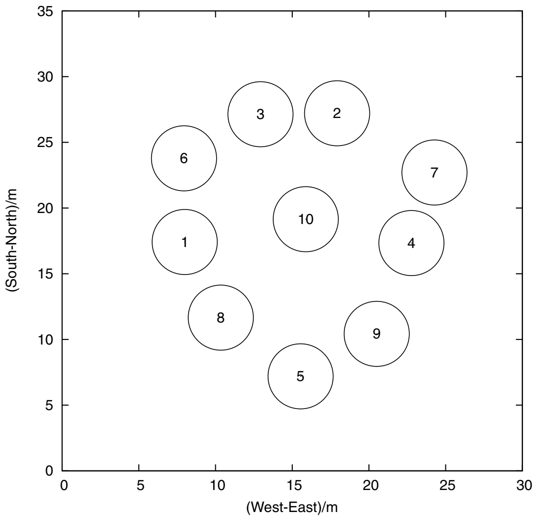

Figure 7. Current SA relative antenna positions in metres.

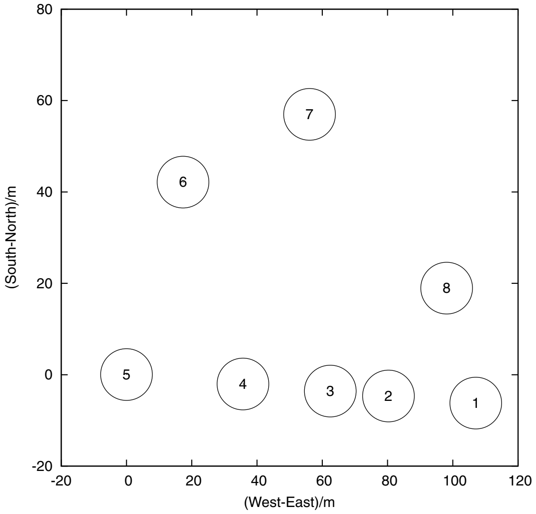

Figure 8. LA relative antenna positions in metres.

The noise temperature of the entire cryostat is 13 K at 15 GHz, rising to 24 K at 12 and 18 GHz. The full system temperature, averaged over 12–18 GHz, is better than 30 K at zenith including the CMB and atmosphere.

4.2 SA feed assembly

The radio frequency (RF) signal from the secondary reflector enters a corrugated feedhorn. The AMI corrugated feedhorns have a circularly symmetric aperture field distribution and low sidelobes (see e.g. Clarricoats & Seng 1973). Attached to the neck of the feedhorn is an adaptor converting circular waveguide to rectangular, resulting in sensitivity to Stokes' parameters $I + Q$, followed by a rectangular waveguide to coaxial converter. Then a cooled isolator before the front-end amplifier ensures a good impedance match to the amplifier and reduces the return loss. The feedhorn must be cooled to 20 K to achieve low receiver noise. Incorporating the entire feedhorn into the cryostat and mounting everything on the vacuum base plate simplifies the assembly. The feedhorn and the first-stage receiver are cooled to 20 K by a closed-cycle helium refrigerator with a 50-K intermediate shield surrounding it (Fig. 9). For the SA we use CTI type 350C two-stage coldheads with cooling powers of 4 W at 21 K and 15 W at 77 K.

The disadvantage of incorporating the feedhorn in the cryostat is the large (120-mm diameter) cryostat window. The window must be transparent over the observational band and must maintain a good vacuum seal under loading by atmospheric pressure, and an IR filter is needed. Two designs were tried (see Kaneko 2005, 2006). A 75-μm mylar weather window (and UV filter) protects the vacuum window from the elements. Distributed dry air is circulated between the two windows in order to prevent water forming on the outside of the vacuum window.

We further found that dew formed on the cryostat weather window during damp nights, typically raising the system temperature by a factor of 5. Dew formation is encouraged by the close proximity (see Fig. 9) of the cooled feedhorn. So to keep the window dry, a second dry-air system directs pressurized dry air over the outer surface of the weather window. This solves the dew problem, as well as drying the windows more quickly after rainfall.

4.3 LA feed assembly

The LA feed assembly (Fig. 10) is based on the RT 15-GHz system. In contrast to the SA feed assembly, the horn is not completely cooled. However, the vacuum window aperture is consequently much smaller and there is no need for an IR filter. There is a thermal break in the horn between the throat and vacuum window. To suppress undesirable mode effects, which were detected as peaks in the cryostat system noise as a function of frequency, the first horn section was fitted with a PTFE dielectric ring, secured in place in the last corrugation closest to the mouth. The SA and LA horns are almost identical in size. As with the SA, the cryostat is cooled to 20 K in the first stage and 50 K in the second, but the LA has CTI type 22C two-stage coldheads with cooling powers of 1.5 W at 21 K and 4 W at 63 K.

5 INTERMEDIATE FREQUENCY SYSTEM

AMI's RF/IF chain is illustrated in Fig. 11. The design is largely common to both arrays.

After the RF signal leaves the cryostat, it is downconverted (Section 5.2) using a local oscillator (LO, Section 5.1), to form the IF band. The total path lengths from the horn to the correlator detector are kept as similar as possible between, and within, antennas throughout the length of the IF chain. The IF amplifier and equalizer units were designed and built in-house, using off-the-shelf amplifier chips bonded to microstrip, because the required performance was not commercially available. The IF passes through the path compensators (PCs, Section 5.3) and automatic gain control (AGC, Section 5.4) before being correlated (Section 6).

5.1 Local oscillator

In both arrays, a 12-GHz dielectric resonance oscillator is phase locked to a 100-MHz reference generated by a crystal oscillator. The LO is then passed through a frequency doubler, and the output is high-pass filtered to reject the original 12-GHz signal. This 24-GHz LO is phase switched (Section 5.2.1) and mixed with the 12–18 GHz RF to yield a single-sideband IF of 6–12 GHz (see Section 5.2). The upper sideband is discarded. The lower sideband (with LO at 24 GHz) is used in preference to the upper sideband (LO at 6 GHz) in order to keep the LO and its harmonics outside

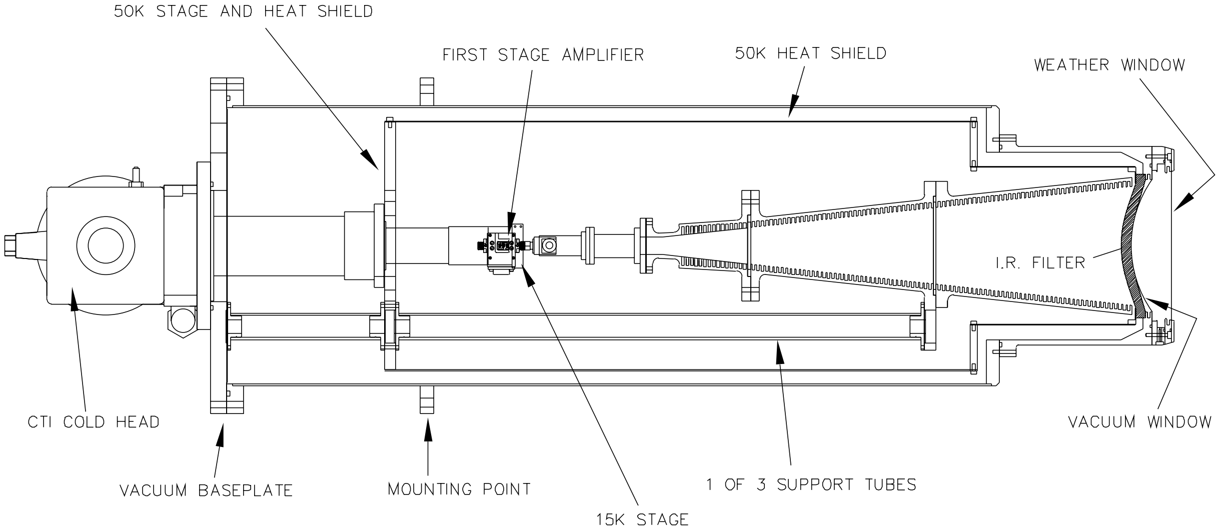

Figure 9. SA cryogenic receiver. The internal diameter of the horn mouth is 108 mm.

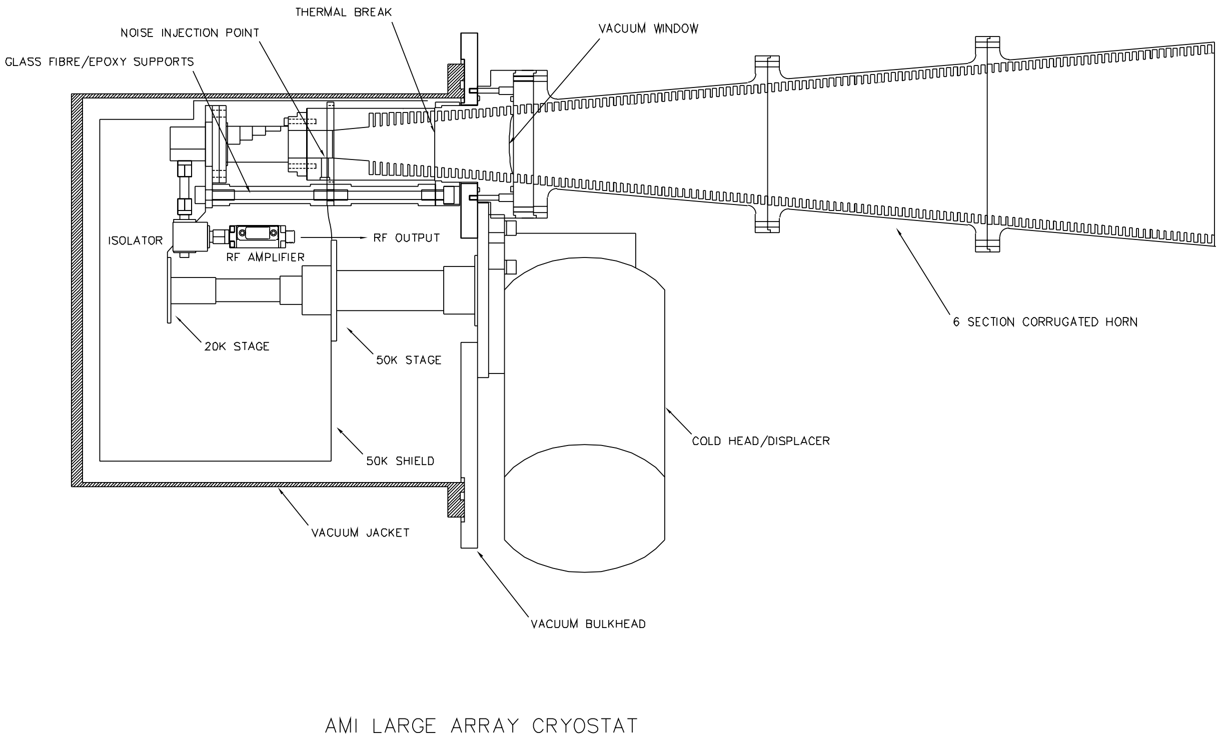

Figure 10. LA cryogenic receiver. The internal diameter of the horn mouth is 106 mm. The horn is in six corrugated sections, including one short section immediately to the right of the vacuum window.

the IF band. A fundamental oscillator at 24 GHz would have been preferred to the doubled 12-GHz system but no suitable device was available.

In the LA, the long LO distribution paths mean that cable losses would be too great to distribute the LO at 12 GHz. Instead, the 100-MHz locking signal is distributed, via UR67 coaxial cable, and each antenna has its own 12-GHz phase-locked oscillator (PLO) and 24-GHz doubler. Each LA downconverter originally had its own AGC to control the 100-MHz power level. Small variations in 100-MHz power were found to have minimal effect on the 24-GHz stability, and the voltage-controlled attenuator was found to be noisy and unstable, so the AGC was removed.

In the SA, the LO distribution paths are shorter and the corresponding 12-GHz cable losses less, so that it is more economical to have a single, central 12-GHz PLO locked to a 100-MHz oscillator, distributed at 12 GHz via Andrews LDF2-50 coaxial cable, with doublers and filters at each antenna.

Bench tests indicated that the LO multiplier units at each LA antenna worked adequately, but when installed they locked only intermittently to the 100-MHz phase-reference signal; this was due

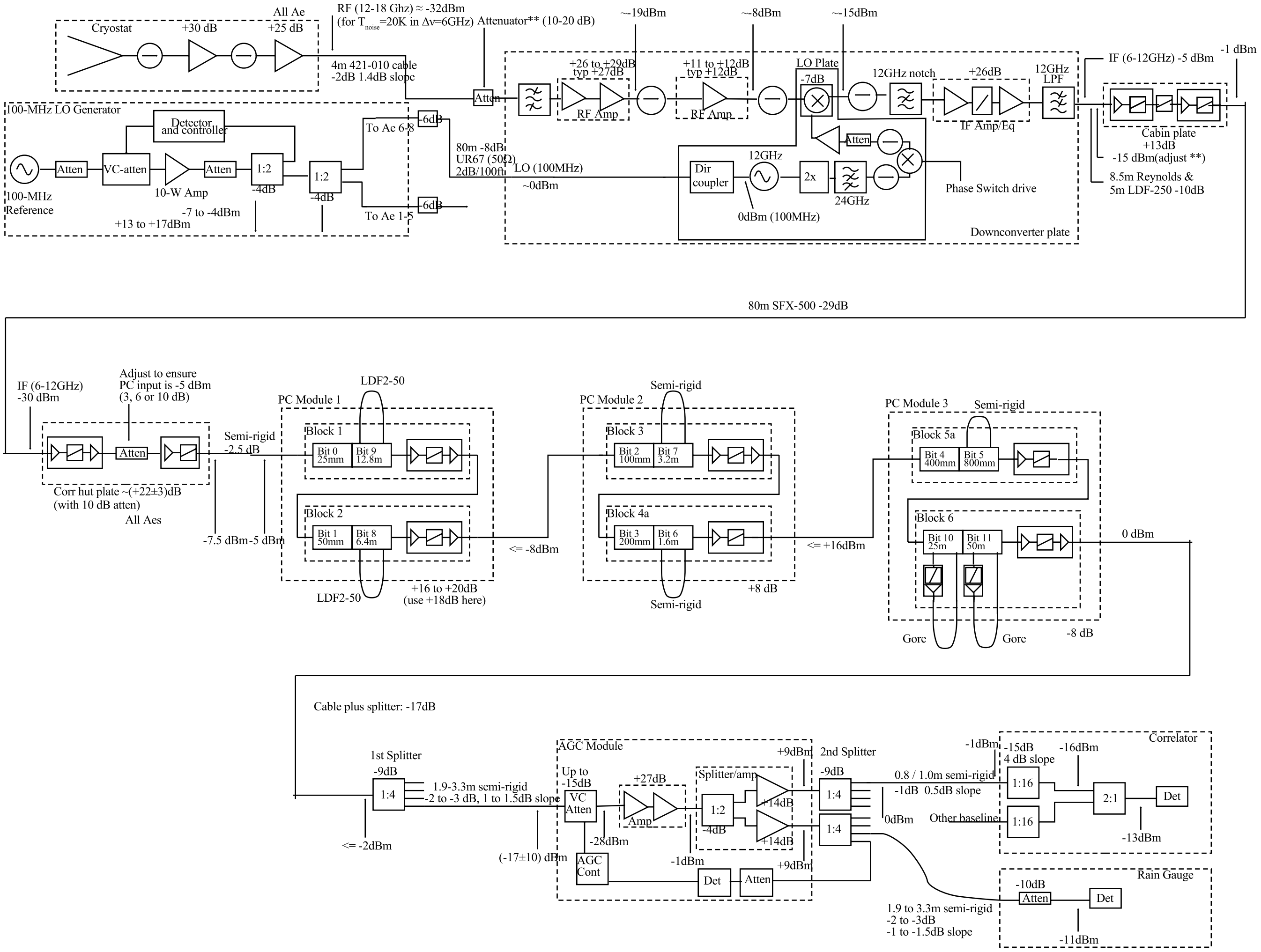

Figure 11. IF chain for the LA. The SA IF chain is very similar, but with a different LO distribution and without the amplifier–equalizer plates either side of the long cable runs, and without the longest two PC bits (see text for details). The attenuator marked ** can be adjusted manually to ensure that the power output levels of the downconversion plates are the same. Power levels are in dBm where 0 dBm = 1 mW.

to their being operated at close to the maximum temperature in their specification, necessitating re-engineering of the downconversion temperature control.

5.2 Downconversion

The RF is sent from the cryostat to the downconversion system via a coaxial cable with microporous Teflon dielectric (Reynolds 421-010 on the SA and Tensolite 301 on the LA). The downconversion system, which includes modules by Atlantic Microwave Ltd, is mounted on a temperature-controlled plate kept to within ±3°C of 35°C in order to reduce temperature-dependent path changes, and, more importantly, to ensure the performance stability of the active components. We undertake downconversion partly because the manufacture of amplifiers, switches and other components is much more economical at lower frequencies. In such a heterodyne system, the instrument's observing frequency can also later be adjusted by adjusting the frequency of the LO.

A bandpass filter on the downconverter plate restricts the bandpass to 12–18 GHz and the RF then passes through two amplifiers and isolators. A 12-GHz notch filter removes any stray LO contamination. Another filter rejects geosynchronous satellite signals around 12.8 GHz.

The IF is transmitted to the correlator room using a 55-m length of Andrews' LDF2-50 cable on the SA and an 80-m length of SFX-500 cable on the LA. At either end of the cable the signal is amplified and equalized to remove the frequency slope due to the cables' increasing loss with frequency.

5.2.1 *Phase switching*

Partly to attenuate spurious signals and the effects of drifts in the signal processing, we introduce 180° phase switching early on in the system (by switching the 24-GHz LO with a known rectilinear waveform) and synchronously detect this switching late in the system after correlation (just before the correlator readout). This process produces the modulation in power of the product signal for each baseline and allows the use of a power detector rather than a multiplier in the correlator (Ryle 1952).

The waveforms used for phase switching are Walsh functions (see e.g. Beauchamp 1984). Their key property is that they are orthogonal, independent of relative phase. We use a different odd-numbered function for each antenna in order to remove the effect of any signal leakage from one radiometer path to another. Walsh functions also make it easy to construct the particular synchronous detection function to apply to each correlation.

The LO is modulated by using a balanced mixer with a DC-coupled IF port – this allows the LO phase to be controlled by injecting a positive or negative current in to this port. A feedback system (see Section 6.3) controls the magnitude of these bias currents such that the amplitude of the LO is equal in each phase state.

We estimate that our phase-switching process reduces spurious signals and drifts by 30 dB.

5.3 Path compensators

Radiation received from a source on the sky takes longer to reach one antenna of a baseline than the other, since one is further from the source. We must continually switch in extra fixed electrical lengths into every antenna IF, thus ensuring that the difference in electrical length between the sky point and correlator by any path is much less than the coherence length of the radiation, $c/\Delta\nu_{\mathrm{ch}}$, where $\Delta\nu_{\mathrm{ch}}$ is the bandwidth of a frequency channel. This is the function of the PCs. Note that because this path compensation is continual rather than continuous, the phase response of an interferometer to the sky point changes at the fringe rate as the earth rotates. Note also that because this path compensation is introduced in the IF whereas the initial path error is in the RF, the phase of the visibility changes at a rate proportional to the change of path length times the difference between the RF and IF frequencies.

On entry to the correlator room of each array, the IF for each antenna passes to the PC modules, where fixed paths of different electrical lengths are switched in.

There are 10 PC bits for each antenna of the SA, with lengths from 25 mm up to 12.8 m. Each bit is nominally slightly less than twice as long as the previous one to ensure that path compensation can be provided for every reachable part of the sky.

The PCs were manufactured in-house as such units are not commercially available. RF switches on a microstrip substrate, controlled by the correlator microprocessor (Section 7), select between a shorter and a longer path for each bit. The equalization and gain of the shorter path are adjusted by placing a piece of Eccosorb above the path's microstrip. In this way, the gain and equalization of the shorter path can be matched to that of the longer to within $\approx$0.5 dB. In order of increasing length, the switched bits are formed from microstrip, aluminium or copper semirigid coaxial cable, Andrews LDF2-50 coaxial cable and, for the longest two bits of the LA only, Gore PRP030306-123 coaxial cables of length 25 and 50 m.

5.4 Automatic gain control

After the PCs, the IF is split passively and equally using Wilkinson dividers. Following the first split, an aluminium semirigid cable takes the IF to an AGC module. The AGC ensures that, despite the time varying and intrinsically different gains of components, as well as varying atmospheric conditions, the IF power entering the correlator is constant to within $\approx$1 dB (in part to ensure that each correlator diode operates efficiently). The AGCs handle an input range of -23 to -3 dBm.

After the AGC, the IF is split again, with one of the splitter outputs returning for the AGC detector loop. The IFs from each pair of antennas then go to two correlator boards (Section 6).

The output of the AGC is sensed by a detector, which feeds back to a Hittite HMC 121 voltage-controlled attenuator. This has better stability, and phase and frequency performance, than a variable-gain amplifier and gives up to 30 dB of control over the IF band. An amplifier is needed to compensate for the attenuator loss. The feedback detector is a coaxial Schottky diode detector (from Advanced Control Components), with a square-law characteristic over the power control range. The detected voltage provides negative feedback control to the voltage-controlled attenuator.

6 CORRELATOR

6.1 RF design

The AMI correlator is an analogue 'add and square' Fourier transform spectrometer (FTS) (for full details see Holler et al. 2007). It splits the 6-GHz band into eight complex frequency channels of 0.75 GHz by correlating the signals of each baseline simultaneously at 16 different discrete delays and then Fourier transforming the measurements in software (a so-called XF correlator, i.e. first correlate, then Fourier transform). The discrete delay length of the lags in the FTS is set by the design bandwidth of 6 GHz and has to satisfy Nyquist's sampling theorem, resulting in a nominal length of 25 mm for each lag.

In general there are two possible architectures for a lag correlator, 'complex' and 'real'. The complex correlator measures amplitude and phase of the detected IF signal at each correlation, using the Nyquist sampling rate for the delay length. The imaginary part is produced by a broad-band 90° phase shift in one antenna. The real correlator measures amplitude only, with half the nominal delay spacing, resulting in the same total number of correlations.

In the 'add and square' design of the FTS the number of detectors has to be doubled in order to reach the same signal-to-noise ratio performance as with a multiplying correlator. For each baseline the sum ('$+$') and difference ('$-$') of the two inputs are formed, the latter using an additional broad-band 180° phase shift in one antenna, and their powers detected with a diode detector. This results in two independent measurements for each lag and the signal-to-noise ratio is increased by $\sqrt{2}$ over a single $+$ or $-$ channel. Previous implementations of similar systems, e.g. the VSA (see Rusholme 2001), combined the $+$ and $-$ correlations in hardware. However, in order to be able to calibrate each for hardware systematics (especially unequal lag spacing) separately, we postpone the combination of $+$ and $-$ signals to the mapping process.

The lags are implemented using microstrip delay lines (Fig. 12). Fluctuations in the dielectric constant of the substrate produce irregularities in the lag spacing, giving an imbalance between the real and imaginary correlated components for each baseline; there are also different intrinsic gains in the detectors and dispersion over the wide band. This leads to a unique frequency response for each correlator, since the mean lag spacing is slightly different and therefore suitable calibration must be applied. Further, the correlator lags are systematically slightly long, which leads to aliasing in the first channel.

The function of each correlator detector is to rectify the IF signal. Ideally, the rectifier output should see a following impedance that is high and purely resistive. A late-stage design change resulted in the diode seeing a largely capacitive load. The use of a series resistor after the diode and the keeping of distance to the input of the following op-amp as short as possible would have given better performance, although even the best-lumped components have resonant frequencies of $\sim$10 GHz. As it is there is substantial loss of sensitivity for the top two IF channels, i.e. the bottom two RF channels. However, due to problems with geostationary satellite

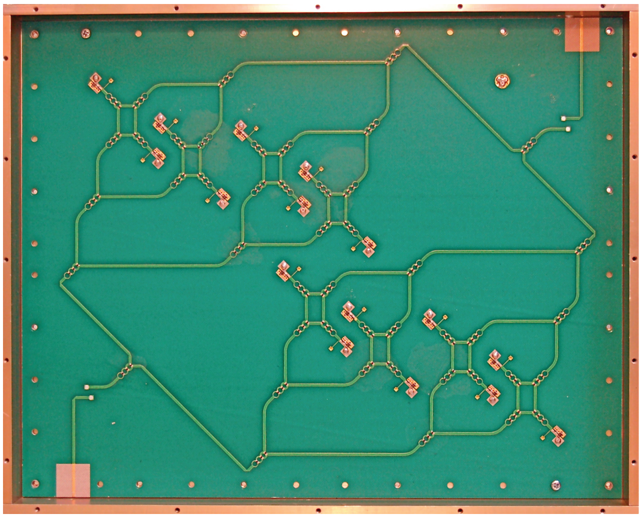

Figure 12. Microstrip correlator (0°). The IFs from the two antennas enter bottom left and top right, before fanning out into a tree of lags. The detectors are at the tips of the branches.

emission, these two channels are currently suppressed anyway by hardware filters.

The SA and LA correlators are identical, but separate. Since each correlator module implements either the + or the − correlation for one baseline the SA has 90 correlators for its 10 antennas, and the LA has 56 correlators for its eight antennas.

6.2 Synchronous monitoring of system temperature

The relative system temperature of each antenna is monitored by a ‘rain gauge’, which detects the power received from amplitude-modulated noise injected by a probe in the circular-waveguide throat of the receiver horn. The increase in the system temperature is negligible from the point of view of overall noise performance, but the injected signal is easily detected by the synchronous power detector. As the system temperature fluctuates due to e.g. gain variations or changing atmospheric emissivity, the AGC adjusts the IF signal amplitude and this decreases or increases the relative amplitude of the modulated noise. The rain gauge measures this and hence the system temperature. All the noise sources are switched with the same Walsh function, which is not one of those used for phase switching.

6.3 Phase-switch balance

A phase-switch balance feedback loop uses a similar method to correct for any amplitude modulation caused by the LO power being different in the two states of the phase-switch mixer (see Section 5.2.1). A synchronous detector generates a feedback signal that is used to bias the mixer control voltages and hence eliminate any amplitude modulation.

6.4 Correlator readout

The readout system is described in Kaneko (2005) and Holler et al. (2007). For each baseline, each pair of correlators is served by two readout cards. The phase-switching signals introduced at downconversion are demodulated and integrated in an analogue circuit, and the signal can then be digitized at a relatively modest rate. We use a 20-bit analogue-to-digital converter to ensure that there is sufficient dynamic range and that the quantization noise is much less than the system noise. Correlators are read out in ‘racks’, each of these consisting of three sets of correlator-readout systems. Each rack interfaces serially to the correlator microprocessor (see Section 7.1).

7 CONTROL SYSTEM

The control systems for the SA and LA are independent realizations of the arrangement illustrated in Fig. 5. At the heart of each is a local Ethernet segment connecting a number of rack-mounted, single-board microprocessors that control the drive and monitoring processes and handle the data stream from the correlator readout. In the case of the SA, these are Eurotech microprocessors (www.arcom.com) running the QNX operating system (www.qnx.com), with a standard desktop computer acting as the master node; the LA control system is a development of this using a later model of Eurotech microprocessors, which run a variant of LINUX rather than QNX. In both cases, the main telescope control system is a Sun workstation which is connected to both the local and wider Ethernets; this runs the user interface, synchronizes telescope control with data readout and deals with the archiving of the raw time-stream data to disk.

7.1 Data acquisition

Data are transmitted as serial digital signals from the correlator racks to the correlator microprocessor, which in the case of the SA is a slave node of the QNX network. The correlator microprocessor samples data at 32 Hz and passes it via Ethernet to a shared memory segment in the Sun workstation, which waits for input.

The only processing steps performed on the data in real time are to remove path-compensator switching transients, by flagging the first two 32-Hz samples when a PC setting changes, and to average samples (over 1 s for the SA and 1/4 s for the LA) before writing to disk in a local data format. Raw data rates from the correlator are of the order of 200 kbps. The data format consists of a header that describes the observation and the telescope configuration, followed by the time-stream data for all active baselines and monitoring information. Each night, the telescope data files are transferred from the observatory to an archive at the Cavendish Laboratory via an optical-fibre data link.

The correlator microprocessor also sets the state of the PC bits, in response to on-the-fly requests from the drive microprocessor. It further reads the rain-gauge data (Section 6.2) via similar analogue-to-digital converters to those for the correlator data.

7.2 Drive control

7.2.1 Small Array

In the SA, a single microprocessor controls the drives for all of the antennas in the array, via a Profibus serial field bus (www.profibus.com/pb). Each antenna has HA and δ Eurotherm servo amplifiers (www.eurotherm.co.uk) and two Heidenhain encoders (one for each axis, www.heidenhain.com), which are devices on the serial bus. The encoders provide a feedback loop for positioning each drive. The logic for limit switches and emergency stop interlocks is handled by relays at each antenna.

Every second, the drive microprocessor fetches the encoder readings (that is, current positions) of all 20 drives from the encoder gateways, determines the speed required to reach the requested encoder positions received from the drive control process in the Sun workstation, and passes these speeds to the servo amplifiers, thus completing the feedback loop. The encoder readings are passed back to the Sun workstation for report and error handling.

Each antenna uses a pair of shielded, dual-core cables to the Profibus standard. The serial bus is completed in the correlator room to allow each antenna to have a dedicated bundle (that includes power, LO, IF, dry air and monitoring cables) for easy repositioning, rather than daisy chaining the antennas directly to each other. An electronic repeater is placed in the correlator room after antenna 5. Active termination of the Profibus was not necessary.

A HA–δ combined south limit switch allows the drives to reach a lower declination than with a single, hard south limit. The elevation limit is $+20^\circ$. The SA antenna slewing speed is $48^\circ\,\mathrm{min}^{-1}$ in HA and $13^\circ\,\mathrm{min}^{-1}$ in δ.

7.2.2 Large Array

Drive control for the LA is similar to that for the SA, except that the LA has one Eurotech drive microprocessor per antenna. Rather than using Profibus, each microprocessor communicates directly with the Eurotherm motor controllers of its respective antenna via an analogue connection.

The other difference is that for the LA, the drive control feedback loop is completed in the Sun workstation. There is a master drive-control task that performs observation control and computes target pointing values for all antennas, and separate independent communications processes for each antenna that compare the actual and required encoder readings each second, compute the appropriate speed commands and transmit these to each microprocessor using a separate Internet-socket connection for each microprocessor. Communication among the control processes in the Sun workstation is via data structures in the shared memory segment. The LA antenna slewing speed is $15^\circ\,\mathrm{min}^{-1}$ in each axis and the elevation limit is $+5^\circ$.

7.3 Monitoring

The cryostat temperature and pressure, the front-end amplifier biases, interlock states and the AGC feedback voltages are relayed to the monitor microprocessor once every second. We also monitor the temperatures of the downconversion plates and the state of the PLO lock. The wind speed is monitored continuously and the LA stowed if the speed reaches a predetermined level.

8 LESSONS LEARNED

In the course of construction, various problems were of course found, such as the need for extra air blowers on the SA (see Section 4.2), the LO locking (Section 5.1), the correlator response, unequally spaced and dispersive lags (Section 6.1). There are three other noteworthy issues.

(i) In this and other telescopes that we have constructed, we have found that often for very simple ‘components’ the manufacturers’ specifications were inadequate to predict actual performance. An example that caused problems in the current context is the operating temperature range of drive-gearbox grease.

(ii) Both real and complex correlators should have identical sensitivities (in the limit of a large number of frequency channels). We prototyped both versions and opted for the real correlator since the RF board was slightly smaller and to obviate small phase errors introduced by the 90° phase shifter. However, this means that full phase information is not available until after the Fourier transform is performed in software. At several points during commissioning having phase information at an earlier stage would have been useful. We advise others considering building this sort of correlator to consider carefully whether to build a real or complex correlator.

(iii) We found that the LDF2-50 cable used on the SA for the IF and longer PC cables had significant dispersion over the AMI band. In the IF, as long as the dispersion of each cable is the same, this did not matter. However, in the PC, in which air path to one telescope is compensated by electrical path in the other, dispersive cable is a problem. We calculated that for PC total lengths in which the longest bit is 12 m, the use of LDF2-50 was acceptable and could be corrected for in software. However, on the LA, where PC cables extend to 50 m, cable of much lower dispersion is essential but proved very difficult to find.

9 PERFORMANCE

Both the SA and the LA have been commissioned. Both arrays meet their design sensitivity, with lower system temperatures compensating for the effect of the loss of the bottom two frequency channels. In 1 h, the SA has a 1σ flux sensitivity of 500 μJy and the LA has a 1σ flux sensitivity of 50 μJy. These sensitivity values are what are expected by scaling from measured RT sensitivity, given antenna area, bandwidth, system temperature and the small loss from the RT 2-bit digital correlator. For integration times over which source contamination is not an issue, we find that the noise from both arrays does indeed integrate down as $\mathrm{time}^{-1/2}$.

Fig. 13 shows a simultaneous observation with both arrays of the cluster Abell 1914 on 2008 May 2 and May 3. The SZ effect from the cluster is clearly visible at the centre of the SA map (Fig. 13a). Both the SA and LA maps show a number of radio point sources; these are unresolved in the SA map, but separated in the LA map (Fig. 13b). The SA observing time was 14 h and the LA map comprises two 10-h rasters of seven and 19 points. The SA map has a 1σ map noise of 150 μJy but has not been CLEANed or corrected for primary beam attenuation; the synthesized beam is $166 \times 152\,\mathrm{arcsec}^2$ with position angle 67°. The LA map has been CLEANed and primary beam corrected, giving a 1σ map noise of 60 μJy; the synthesized beam is $38 \times 29\,\mathrm{arcsec}^2$ with position angle 28°. The LA observations used just six of the eight antennas, as two antennas were out of service.

ACKNOWLEDGMENTS

We thank PPARC/STFC and Cambridge University for AMI construction and operation. TLC, MLD, TMOF, NH-W, TK, KL, PJM, CR-G, AMMS, TWS and JTLZ acknowledge PPARC/STFC studentships. FF acknowledges support from the Cambridge Commonwealth Trust and the Cambridge Isaac Newton Trust, JG acknowledges support from the Cambridge Isaac Newton Trust and the Cambridge European Trust, JCP acknowledges support from the Cambridge Overseas Trust and MV acknowledges support from the Gates Cambridge Trust. We thank Paul Alexander and Steve Rawlings, and we also thank the referee Mark Birkinshaw for useful comments and suggestions. We thank staff at NRAO Charlottesville for help with the front-end amplifiers. We are also grateful to Atlantic Microwave Ltd, Castle Microwave Ltd, W. L. Gore & Associates Inc., Steven Hardwick Associates Ltd and Prima

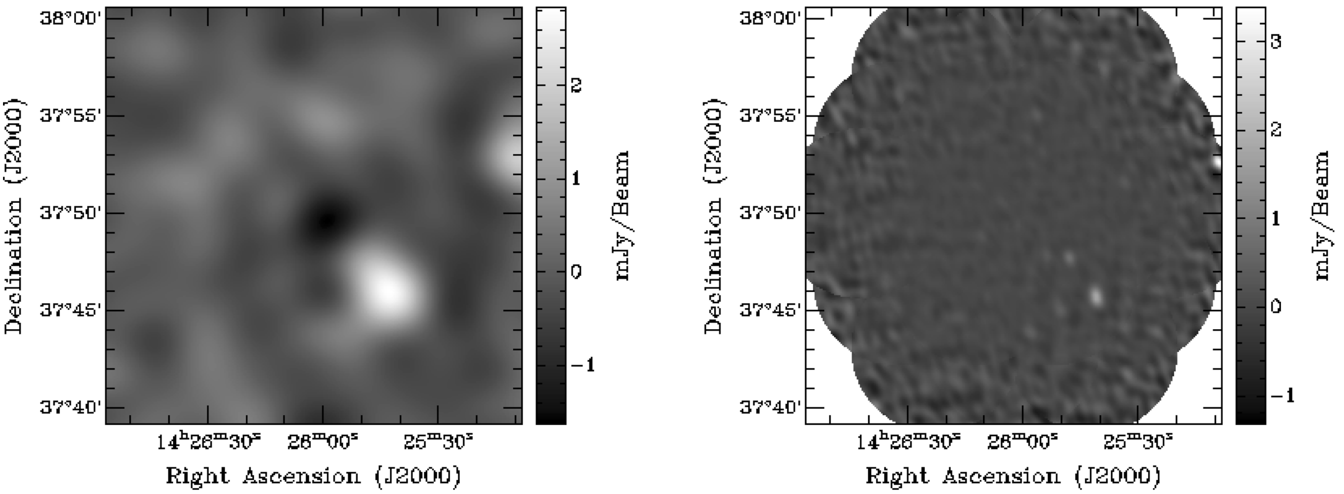

(a) Single-pointing SA map.

(b) LA map comprising a 7- and 19-point raster.

Figure 13. A simultaneous 2-d observation of Abell 1914 with AMI. See Section 9 for details of the observations and maps.

Electronic Services Ltd for their excellent technical understanding and assistance.

REFERENCES

AMI Collaboration, 2006, MNRAS, 369, L1
Bartlett J. G., Silk J., 1994, ApJ, 423, 12
Beauchamp K. G., 1984, Applications of Walsh and Related Functions. Academic Press, London
Birkinshaw M., 1999, Phys. Rep., 310, 97
Birkinshaw M., Gull S. F., Moffet A. T., 1981, ApJ, 251, L69
Birkinshaw M., Gull S. F., Hardebeck H., 1984, Nat, 309, 34
Bonamente M., Joy M. K., LaRoque S. J., Carlstrom J. E., Reese E. D., Dawson K. S., 2006, ApJ, 647, 25
Bond J. R., Myers S. T., 1992, in Cline D., Peccei R., eds, Trends in Astroparticle Physics. World Scientific, Singapore, p. 262
Cantalupo C. M., Romer A. K., Peterson J. B., Gomez P., Griffin G., Newcomb M., Nichol R. C., 2002, preprint (astro-ph/0212394)
Carlstrom J. E., Joy M., Grego L., 1996, ApJ, 456, L75
Carlstrom J. E., Holder G. P., Reese E. D., 2002, ARA&A, 40, 643
Church S. E., 1995, MNRAS, 272, 551
Clarricoats P. J. B., Seng L. M., 1973, Electron. Lett., 9, 7
Cotter G. et al., 2002a, MNRAS, 331, 1
Cotter G., Buttery H. J., Das R., Jones M. E., Grainge K., Pooley G. G., Saunders R., 2002b, MNRAS, 334, 323
Dobbs M., Halverson N. W., Ade P. A. R., Basu K., Beelen A., Bertoldi F., Cohalan C., 2006, New Astron. Rev., 50, 960
Galindo V., 1964, IEEE Trans. Antennas Propag., 12, 403
Geisbüsch J., Kneissl R., Hobson M., 2005, MNRAS, 360, 41
Grainge K., Jones M., Pooley G., Saunders R., Baker J., Haynes T., Edge A., 1996, MNRAS, 278, L17
Grainge K., Grainger W. F., Jones M. E., Kneissl R., Pooley G. G., Saunders R., 2002a, MNRAS, 329, 890
Grainge K., Jones M. E., Pooley G., Saunders R., Edge A., Grainger W. F., Kneissl R., 2002b, MNRAS, 333, 318
Grainger W. F., Das R., Grainge K., Jones M. E., Kneissl R., Pooley G. G., Saunders R. D. E., 2002, MNRAS, 337, 1207
Grego L., Carlstrom J. E., Joy M. K., Reese E. D., Holder G. P., Patel S., Cooray A. R., Holzapfel W. L., 2000, ApJ, 539, 39
Herbig T., Lawrence C. R., Readhead A. C. S., Gulkis S., 1995, ApJ, 449, L5
Holler C. M., Kaneko T., Jones M. E., Grainge K., Scott P., 2007, A&A, 464, 795
Holler C. M., Hills R. E., Jones M. E., Grainge K., Kaneko T., 2008, MNRAS, 384, 1207
Holzapfel W. L., Wilbanks T. M., Ade P. A. R., Church S. E., Fischer M. L., Mauskopf P. D., Osgood D. E., Lange A. E., 1997, ApJ, 479, 17
Jones M. E., 2002, in Chen L.-W., Ma C.-P., Ng K.-W., Pen U.-L., eds, ASP Conf. Ser. Vol. 257, AMiBA 2001: High-Z Clusters, Missing Baryons, and CMB Polarization. Astron. Soc. Pac., San Francisco, p. 35
Jones M. E. et al., 1993, Nat, 365, 320
Jones M. E. et al., 2005, MNRAS, 357, 518
Joy M. et al., 2001, ApJ, 551, L1
Kaneko T., 2005, PhD thesis, Univ. Cambridge
Kaneko T., 2006, SPIE, 6267, 124
Keto E., 1997, ApJ, 475, 843
Kneissl R., Jones M. E., Saunders R., Eke V. R., Lasenby A. N., Grainge K., Cotter G., 2001, MNRAS, 328, 783
Korolev V. A., Sunyaev R. A., Yakubtsev L. A., 1986, Sov. Astron. Lett., 12, 141
Kosowsky A., 2006, New Astron. Rev., 50, 969
Lancaster K., 2004, PhD thesis, Univ. Cambridge
Lancaster K. et al., 2005, MNRAS, 359, 16
Lancaster K. et al., 2007, MNRAS, 378, 673
LaRoque S. J., Bonamente M., Carlstrom J. E., Joy M. K., Nagai D., Reese E. D., Dawson K. S., 2006, ApJ, 652, 917
Lay O. P., Halverson N. W., 2000, ApJ, 543, 787
Li C.-T. et al., 2006, SPIE, 6275, 49
Lin Y.-T., Partridge B., Pober J. C., El Bouchefry K., Burke S., Klein J., Coish J., Huffenberger K., 2008, preprint (astro-ph/0805.1750)
Mason B. S. et al., 2003, ApJ, 591, 540
Muchovej S. et al., 2007, ApJ, 663, 708
Patel S. K. et al., 2000, ApJ, 541, 37
Pospieszalski M. W., 2005, Microw. Mag., 6, 62
Reese E. D. et al., 2000, ApJ, 533, 38
Reese E. D., Carlstrom J. E., Joy M., Mohr J. J., Grego L., Holzapfel W. L., 2002, ApJ, 581, 53
Robson M., O'Sullivan C. M. M., Scott P. F., Duffett-Smith P. J., 1994, A&A, 286, 1028
Rossetti M., Ghizzardi S., Molendi S., Finoguenov A., 2007, A&A, 463, 839
Ruhl J. et al., 2004, SPIE, 5498, 11

Rusholme B. A., 2001, PhD thesis, Univ. Cambridge
Ryle M., 1952, Proc. R. Soc. A, 211, 351
Ryle M., 1972, Nat, 239, 435
Sanders J. S., Fabian A. C., 2007, MNRAS, 381, 1381
Saunders R. et al., 2003, MNRAS, 341, 937
Sunyaev R. A., Zeldovich Y. B., 1970, Comments Astrophys. Space Phys., 2, 66
Sunyaev R. A., Zeldovich Y. B., 1972, Comments Astrophys. Space Phys., 4, 173
Udomprasert P. S., Mason B. S., Readhead A. C. S., Pearson T. J., 2004, ApJ, 615, 63
Uson J. M., 1986, in O'Dea C. P., Uson J. M., eds, Radio Continuum Processes in Clusters of Galaxies. National Radio Astronomy Observatory, Charlottesville, p. 255
Waldram E. M., Pooley G. G., Grainge K. J. B., Jones M. E., Saunders R. D. E., Scott P. F., Taylor A. C., 2003, MNRAS, 342, 915
Webber J. C., Pospieszalski M. W., 2002, IEEE Trans. Microw. Theory Tech., 50, 986
Zwart J. T. L., 2007, PhD thesis, Univ. Cambridge

This paper has been typeset from a TEX/LATEX file prepared by the author.